AALBORG UNIVERSITY

DENMARK

Magnetic integration of the harmonic filter inductor for dual-converter fed open-end transformer topology

Gohil, Ghanshyamsinh Vijaysinh; Bede, Lorand; Teodorescu, Remus; Kerekes, Tamas; Blaabjerg, Frede

Magnetic Integration of the Harmonic Filter Inductor for Dual-Converter Fed Open-End Transformer Topology

Ghanshyamsinh Gohil, Lorand Bede, Remus Teodorescu, Tamas Kerekes, Frede Blaabjerg
Department of Energy Technology, Aalborg University, Denmark
gvg@et.aau.dk

Abstract—**Many high power converter systems are often connected to the medium voltage network using a step-up transformer. In such systems, the converter-side windings of the transformer can be configured as an open-end and multi-level voltage waveforms can be achieved by feeding these open-end windings from both ends using the dual-converter. An LCL filter with separate converter-side inductors for each of the converter is commonly used to attenuate the undesirable harmonic frequency components in the grid current. The magnetic integration of the converter-side inductors is presented in this paper, where the flux in the common part of the magnetic core is completely canceled out. As a result, the size of the magnetic component can be significantly reduced. A multi-objective design optimization is presented, where the energy loss and the volume are optimized. The optimization process takes into account the yearly load profile and the energy loss is minimized, rather than minimizing the losses at a specific operating point. The size reduction achieved by the proposed inductor is demonstrated through a comparative evaluation. Finally, the analysis is supported through simulations and experimental results.**
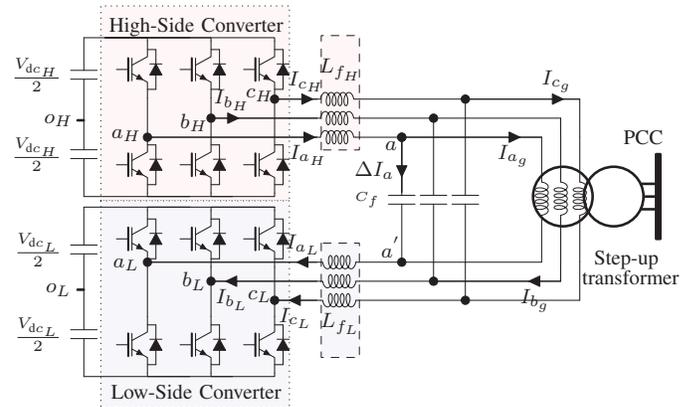
Fig. 1. The system configuration of the dual converter fed open-end winding transformer topology with two separate dc-links. The open-end primary windings are fed from two-level voltage source converters.

I. INTRODUCTION

Many high power converter systems are often connected to the medium voltage network and a step-up transformer is used to match the voltage levels of the converter with the medium voltage grid. In some applications, the transformer is also required for providing galvanic isolation. In such systems, the converter-side windings of the transformer can be configured as an open-end. This open-end transformer winding can be fed from both the ends using the two-level Voltage Source Converters (VSCs) [1], as shown in Fig. 1. The number of levels in the output voltages is the same as that of the three level Neutral point clamped (NPC) converter and each of the two-level VSC operates with the half of the dc-link voltage than the dc-link voltage required for the three level NPC. However, Common Mode (CM) circulating current flows through the closed path if both the VSCs are connected to a common dc-link. The CM circulating current can be suppressed either by using the CM choke [2], [3] or by employing a proper Pulse Width Modulation (PWM) scheme to ensure complete elimination of the CM voltage [4], [5]. However, in many applications, isolated dc-links can be derived from the source itself and such extra measures for CM circulating current suppression may not be required. For example, the isolated dc-links can be obtained in

1) PhotoVoltaic (PV) systems by dividing the total number of arrays into two groups to form separate dc-links [1].
2) Wind Energy Conversion System (WECS): isolated dc-links can be obtained by using a dual stator-winding generator [6].

Therefore the analysis presented in this paper is mainly focused on the dual converter fed open-end transformer topology with two separate dc-links.

An LCL filter is commonly used in high power grid-connected applications [7] and one of the possible arrangement of the LCL filter for the dual-converter fed open-end transformer topology is shown in Fig. 1. The leakage inductance of the transformer is used as a grid-side inductor of the LCL filter. Two VSCs (denoted as High-Side Converter (HSC) and Low-Side Converter (LSC) in Fig. 1) are connected to a common shunt capacitive branch of the LCL filter through the converter-side inductors L_{f_H} and L_{f_L}, respectively. The magnetic integration of the L_{f_H} and L_{f_L} is presented in this paper. As a result of this magnetic integration, the flux in the common part of the magnetic core is completely canceled out. This leads to substantial reduction in the size of the converter-side inductor.

This paper is organized as follows: The operation principle of the dual-converter fed open-end transformer topology is
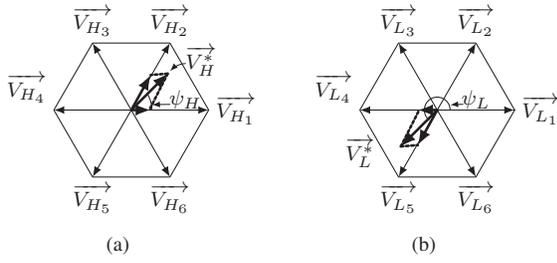
Fig. 2. Reference voltage space vector and its formation by the geometrical summation. (a) Reference voltage space vector for the HSC, (b) Reference voltage space vector for the LSC.
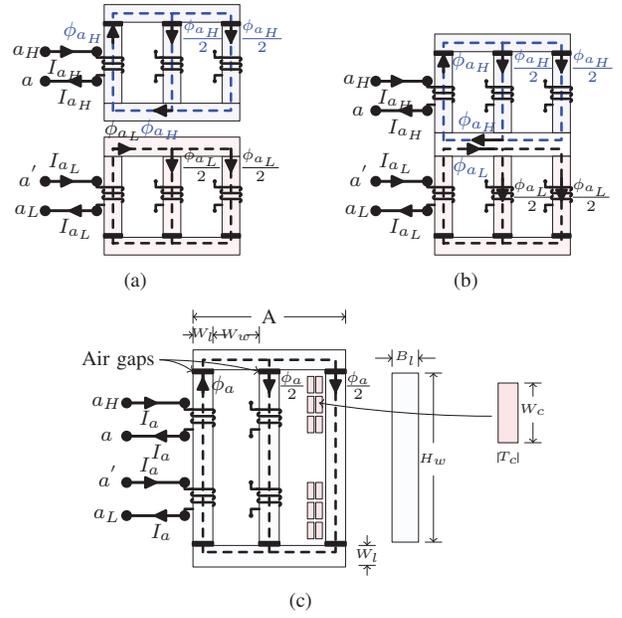

Fig. 3. Magnetic structure. (a) Separate inductors for the HSC and the LSC, (b) Flux cancellation through magnetic integration, (c) Proposed integrated inductor.

briefly discussed in Section II. The magnetic structure of the proposed integrated inductor is described in Section III. Section IV discusses the design procedure in general and the multi-objective optimization of the integrated inductor. The size reduction achieved by the magnetic integration is also demonstrated by comparing the volume of the integrated inductor with the separate inductor case for the 6.6 MVA, 3.3 kV WECS and it is presented in Section V. The simulation and the experimental results are finally presented in Section VI.

II. DUAL-CONVERTER FED OPEN-END TRANSFORMER TOPOLOGY

The operation of the dual-converter fed open-end transformer converter is briefly described in this section. The dual-converter system consists of the HSC and the LSC is shown in Fig. 1. A Two-level VSC is used for both the HSC and the LSC. However, the discussion presented in this paper is also applicable to other converters as well.

The reference voltage space vector $\overrightarrow{V^*}$ is synthesized by modulating the HSC and the LSC. The magnitude of the reference voltage space vectors of the HSC and the LSC is half than that of the desired reference voltage space vector $\overrightarrow{V^*}$ ($|\overrightarrow{V_H^*}| = |\overrightarrow{V_L^*}| = |\overrightarrow{V^*}|/2$). The reference voltage space vector angle of the HSC is kept the same as that of the desired voltage space vector ($\psi_H = \psi$), whereas the reference voltage space vector angle of the LSC is shifted by an angle $180°$ ($\psi_L = \psi_H + 180°$), as shown in Fig. 2.

From Fig. 1, the voltage across the shunt capacitive branch C_f of the LCL filter is given as

$$V_{xx'} = (V_{x_H o_H} - V_{x_L o_L}) - L_{f_H}\frac{dI_{x_H}}{dt} - L_{f_L}\frac{dI_{x_L}}{dt} + V_{o_H o_L} \quad (1)$$

where the subscript x represents the phases $x = \{a, b, c\}$. As the dc-links are separated, the common-mode components of the voltages in (1) do not drive any common-mode circulating current. As a result, only the differential mode current would flow through the inductors. For the dual converter system, these currents are equal.

$$I_{x_H} = I_{x_L} = I_x \quad (2)$$

where I_{x_H} and I_{x_L} are the currents in the phase x of the HSC and LSC, respectively. Assuming $L_{f_H} = L_{f_L} = L_f/2$

and using (1) and (2), the voltage across the converter-side inductor is given as

$$L_f \frac{dI_x}{dt} = (V_{x_H o_H} - V_{x_L o_L}) - V_{xx'} + V_{o_H o_L} \quad (3)$$

where L_f is the equivalent converter-side inductance of the LCL filter. A single magnetic component with the inductance L_f is realized by the magnetic integration of the L_{f_H} and L_{f_L} and the structure is discussed in the following section.

III. INTEGRATED INDUCTOR

In this paper, a three-phase inductor is chosen for the illustration due its wide-spread use in the high power applications. However, it is important to point out that the same analysis can be used for the single-phase inductor as well. The three-phase three-limb converter-side inductor for both the HSC and the LSC are shown in Fig. 3(a). These two inductors can be magnetically integrated as shown in Fig. 3(b), where both the inductors share a common magnetic path. The magnetic structure has six limbs, on which the coils are wound. The upper three limbs belong to the L_{f_H}, whereas the lower three limbs receive the coils corresponding to the L_{f_L}. The upper limbs are magnetically coupled using the top bridge yoke, whereas the lower three limbs are magnetically coupled using the bottom bridge yoke. The upper and the lower limbs share a common yoke, as shown in Fig. 3(b).

Considering three-phase three-wire system

$$I_a + I_b + I_c = 0 \quad (4)$$

and at a particular instance
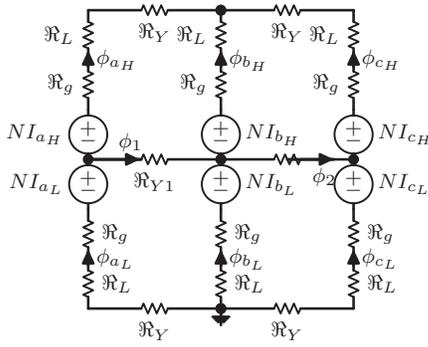
$$I_a = -(I_b + I_c) \quad (5)$$

Fig. 4. Simplified reluctance model of the magnetic structure shown in Fig. 3(b).

The flux distribution in the magnetic structure for this case (the positive value of the I_a and the negative values of the I_b and I_c) is shown in Fig. 3(b). The simplified reluctance model of this magnetic structure is shown in Fig. 4, where $\Re_L$, $\Re_g$, and $\Re_Y$ are the reluctances of the limb, the air gap, the top and the bottom bridge yokes, respectively. The reluctance of the common yoke is represented as $\Re_{Y1}$. ϕ_{a_H}, ϕ_{b_H}, and ϕ_{c_H} are the fluxes in the upper three limbs whereas ϕ_{a_L}, ϕ_{b_L}, and ϕ_{c_L} are the fluxes in the lower three limbs. ϕ_1, and ϕ_2 represent the fluxes in the common yokes, as shown in Fig. 4. By solving the reluctance network, the fluxes in various parts of the integrated inductor are obtained and they are given as

$$\phi_{a_H} = \frac{NI_{a_H}}{\Re_g + \Re_L + \Re_Y}, \; \phi_{a_L} = \frac{NI_{a_L}}{\Re_g + \Re_L + \Re_Y} \quad (6)$$

$$\phi_{c_H} = \frac{NI_{c_H}}{\Re_g + \Re_L + \Re_Y}, \; \phi_{c_L} = \frac{NI_{c_L}}{\Re_g + \Re_L + \Re_Y} \quad (7)$$

and

$$\phi_{b_H} = \frac{NI_{b_H}}{\Re_g + \Re_L}, \; \phi_{b_L} = \frac{NI_{b_L}}{\Re_g + \Re_L}, \; \phi_1 = 0, \; \phi_2 = 0 \quad (8)$$

The flux components in the common yoke (ϕ_1 and ϕ_2) are zero and therefore the common yoke can be completely removed, as shown in Fig. 3(c). The integrated inductor has only two yokes, compared to four in the case of the separate inductors. As a result, substantial reduction in the volume of the inductor can be achieved through magnetic integration of L_{f_H} and L_{f_L}.

By analyzing the magnetic structure shown in Fig. 3(c) and neglecting the asymmetry introduced by the three-limb structure (by neglecting $\Re_Y$), the value of the L_f is obtained as

$$L_f = \frac{4N^2}{2\Re_g + 2\Re_L} \quad (9)$$

The reluctance of the air gap is generally large compared to the reluctance of the magnetic material. Therefore, simplified expression for the converter side filter inductor is given as

$$L_f \approx \frac{2N^2}{\Re_g} \approx \frac{2\mu_0 N^2 A_g'}{l_g} \quad (10)$$

where μ_0 is the permeability of the free space, l_g is the length of the air gap (of upper/bottom limb) and A_g' is the effective

Parameters	Simulations	Experiment
Power S	6.6 MVA (6 MW)	11 kVA (10 kW)
Switching frequency f_{sw}	900 Hz	900 Hz
AC voltage (line-to-line) V_{ll}	3300 V	400 V
Rated current	1154 A	15.8 A
DC-link voltage ($V_{dc_H} = V_{dc_L}$)	2800 V	330 V
Modulation index range	$0.95 \leq M \leq 1.15$	$0.95 \leq M \leq 1.15$
Transformer leakage L_g	525 μH (0.1 pu)	4.2 mH (0.1 pu)
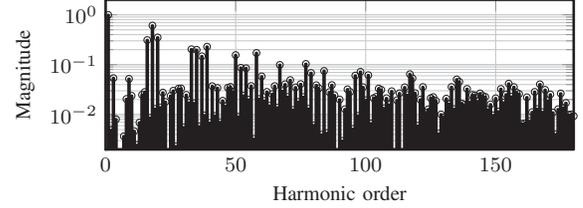
(a)
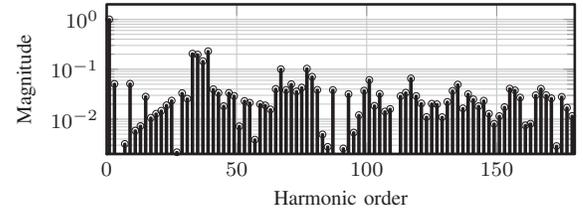
(b)

Fig. 5. Simulated harmonic spectrum of the switched voltages with the modulation index $M = 1$ and the switching frequency of 900 Hz. (a) Switched output voltage of the high-side converter $V_{a_H o_H}$ (normalized with respect to the $V_{dc}/2$), (b) Resultant voltage ($V_{a_H o_H} - V_{a_L o_L}$) (normalized with respect to the V_{dc}).

cross-sectional area of the air gap after considering the effects of the fringing flux. The effective cross-sectional area of the air gap $A_{g'}$ is obtained by evaluating the cross-section area of the air gap after adding l_g to each dimension in the cross-section.

IV. DESIGN OF THE INTEGRATED INDUCTOR

A design methodology is demonstrated in this section by carrying out the design of the integrated inductor for the high power WECS. The system specifications of the WECS is given in Table I. The WECS operates with the power factor close to unity and in this case, the $60°$ Discontinuous Pulse-Width Modulation (commonly referred to as a DPWM1 [8]) scheme could result up to 50% switching loss reduction compared to the continuous modulation scheme. Therefore DPWM1 is used to modulate the HSC and the LSC. Using this specifications, the design of the integrated inductor is carried out and the design steps are illustrated hereafter.

A. Obtain the value of the converter-side inductor L_f

The harmonic spectra of the switched output voltage of the HSC is shown in Fig. 5(a). The major harmonic components in the switched output voltage of the individual converter

appears at the carrier frequency, whereas these components are substantially reduced in the resultant voltage, as shown in Fig. 5(b). The spectrum comprises the maximum values of the individual voltage harmonic components of the resultant voltage, over the entire operating range is obtained and it is defined as a Virtual Voltage Harmonic Spectrum (VVHS) [9]. Using VVHS, the required admittance for the hth harmonic component is obtained as

$$Y_h^* = \frac{I_{h,BDEW}^*}{V_{h,VVHS}} \tag{11}$$

where $I_{h,BDEW}^*$ is the specified BDEW current injection limit of the hth harmonic component (refer to [10]) and $V_{h,VVHS}$ is the maximum values of the hth harmonic components over the entire operating range. The value of the filter parameters are then chosen such that the designed filter has a lower admittance than the required value of the filter admittance for all the harmonic frequency components of interest (upto 180th harmonic frequency component in case of the BDEW standard) [11]. Once the value of L_f is obtained, an optimized design can be carried out.

B. Core Loss Modeling

The Improved Generalized Steinmetz Equation (IGSE) [12], [13] is used to calculate the core losses. The core losses per unit volume is given as

$$P_{fe,v} = \frac{1}{T} \int_0^T k_i \left| \frac{dB(t)}{dt} \right|^\alpha (\Delta B)^{\beta - \alpha} dt \tag{12}$$

where α, β and k_i are the constants determined by the material characteristics. ΔB is the peak-to-peak value of the flux density and T is the switching interval. The flux waveform has major and minor loops and these loops are evaluated separately.

1) Major Loop: Assuming the inductance value to be constant, the flux density in the limb corresponding to the phase x is given as

$$B_x(t) = \frac{L_f I_{x,f}(t)}{2NA_c} \tag{13}$$

where A_c is the cross-sectional area of the limb, $I_{x,f}$ is the fundamental component of the current.

2) Minor Loop: The reference space vector $\vec{V_H^*}$ and $\vec{V_L^*}$ are synthesized using active and zero voltage vectors and the volt-second balance is maintained by choosing appropriate dwell time of these vectors. The application of the discrete vectors results in an error between the applied voltage vector and the reference voltage vector, as shown in Fig. 6 for the HSC. Similarly, the error voltage vectors for the LSC also exists due to the finite sampling. These error voltage vectors lead to the minor loop in the flux density waveform and it is evaluated by performing time integral of the error voltage vector.

The time integral of the error voltage vector is known as the harmonic flux vector [14], [15] and the difference of the harmonic flux vectors of the HSC and the LSC are
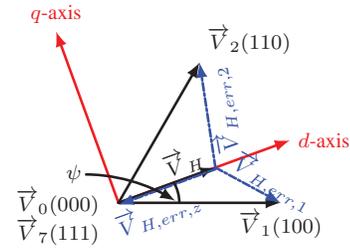

Fig. 6. The active and zero vectors to synthesize given reference vector and corresponding error voltage vectors.

directly proportional to the flux in the integrated inductor. In the reference frame, rotating synchronously at the fundamental frequency, the instantaneous error voltage vectors can be decomposed into d-axis and the q-axis components and they are for the HSC given as (see Fig. 6)

$$\vec{V}_{H,err,1} = \frac{2}{3} V_{dc} \{ (\cos \psi_H - \frac{3}{4} M) - j \sin \psi_H \}$$
$$\vec{V}_{H,err,2} = \frac{2}{3} V_{dc} \{ [\cos(60° - \psi_H) - \frac{3}{4} M] \tag{14}$$
$$+ j \sin(60° - \psi_H) \}$$
$$\vec{V}_{H,err,z} = -\frac{1}{2} V_{dc} M$$

Similarly, the d-axis and the q-axis components of instantaneous error voltage vectors of the LSC are also obtained. Then the difference of the d-axis components of the harmonic flux vectors of the HSC and LSC and the difference of the q-axis components of the harmonic flux vectors of the HSC and LSC are evaluated separately as

$$B_{ac,d}(t) = \frac{1}{2NA_c} \int (\vec{V}_{H,err,d} - \vec{V}_{L,err,d}) dt$$
$$B_{ac,q}(t) = \frac{1}{2NA_c} \int (\vec{V}_{H,err,q} - \vec{V}_{L,err,q}) dt \tag{15}$$

Using the d-axis and the q-axis components, the ripple component of the flux density in the limb corresponding to the phase a is obtained as

$$B_a = B_{ac,d} \cos \psi - B_{ac,q} \sin \psi \tag{16}$$

The VSCs are assumed to be modulated using the asymmetrical regularly sampled PulseWidth Modulation (PWM), where the reference voltage space voltage vector is sampled twice in a carrier cycle.

Using this information, the core loss calculations have been carried out for the major loop and each of the minor loops.

C. Copper Loss Modeling

The copper loss is evaluated by considering the ac resistance of the winding, which takes into account the skin and proximity effects [16]. The total winding losses due to the harmonic frequency components of the coil current is [17]

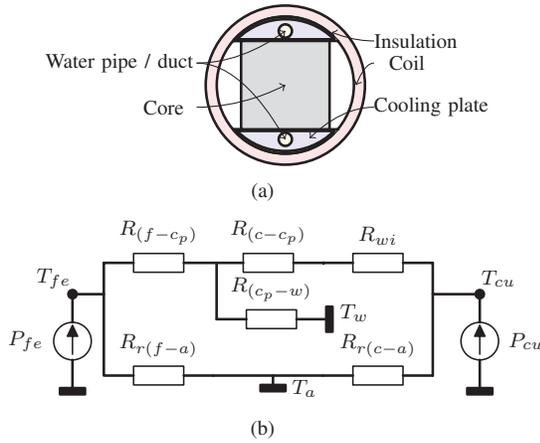$$P_{cu} = R_{dc} \sum_{h=1}^{\infty} k_{p_h} I_{x_h}^2 \tag{17}$$

(a)

(b)

Fig. 7. Simplified thermal model of the integrated inductor. P_{fe} and P_{cu} are the core and copper losses, respectively.

where

$$k_{p_h} = \sqrt{h}\Delta\left[\frac{\sinh(2\sqrt{h}\Delta) + \sin(2\sqrt{h}\Delta)}{\cosh(2\sqrt{h}\Delta) - \cos(2\sqrt{h}\Delta)} + \frac{2}{3}(m^2 - 1)\frac{\sinh(\sqrt{h}\Delta) - \sin(\sqrt{h}\Delta)}{\cosh(\sqrt{h}\Delta) + \cos(\sqrt{h}\Delta)}\right] \quad (18)$$

and $\Delta = T_c/\delta$ and R_{dc} and R_{ac} are the dc and the ac resistance of the coil, respectively. m is the number of layers in the coil, T_c is the thickness of the conductor, and δ is the skin depth. I_{x_h} is the hth harmonic frequency component of the line current I_x. The harmonic spectrum of the resultant voltage is obtained analytically [18] and the hth harmonic frequency component of the line current I_x is obtained as

$$I_{x_h} = Y_{H,LCL}V_h \quad (19)$$

where V_h is the hth harmonic frequency component of the resultant voltage and $Y_{H,LCL}$ is the admittance offered by the *LCL* filter to the hth harmonic frequency component.

D. Thermal Modeling

The liquid cooling of the inductor is considered. The cooling arrangement is shown in Fig. 7(a). The semi-circular aluminum cooling plates with the duct to carry the coolant is considered. This cooling plate is electrically insulated using the epoxy resin. As the heat transfer is anisotropic for the laminated steel, two cooling plates along the edges that are perpendicular to the lamination direction are considered. The hot spot temperature in both the core and the coil (T_{fe} and T_{cu}, respectively) is estimated using the equivalent thermal resistance network [19], shown in Fig. 7(b). For the simplicity of the analysis, the temperature in the core and the coil is assumed to be homogeneous.

The heat transfer mechanism due to the convection and the radiation is considered, where $R_{cv(f-w)}$ and $R_{cv(c-w)}$ are the convection thermal resistance between the core and coolant (water) and between the coil and coolant, respectively. Similarly, $R_{r(f-a)}$ and $R_{r(c-a)}$ represent the radiation thermal

resistance between the core and the ambient and between the coil and the ambient, respectively. The radiation thermal resistance value is obtained using the formulas presented in [19].

The thermal resistance between the cooling plate and the coolant is given as

$$R_{(c_p-w)} = \frac{1}{h_{c_p-w}A_{c_p-w}} \quad (20)$$

where h_{c_p-w} is the heat transfer coefficient and A_{c_p-w} is the coolant contact surface. The heat transfer coefficient is

$$h_{c_p-w} = 3130\left(\frac{q}{785.4D_d^2}\right)^{0.87}(100D_d)^{-0.13} \quad (21)$$

where q is the coolant flow rate in [l/s] and D_d is the diameter of the duct in [m]. The thermal resistance between the core and duct surface is given as

$$R_{(f-c_p)} = \frac{2L_{eq}}{\lambda_{cp}(A_{c_pf} + \pi D_d L_d)} + \frac{T_i}{\lambda_i A_{c_pf}} \quad (22)$$

where L_{eq} is the equivalent distance from the cooling surface to the duct, A_{c_pf} is the contact area of the cooling plate with the core, L_d is the length of the duct, and λ_{cp} is the thermal conductivity of the aluminum. T_i is the thickness of the insulation and λ_i is the thermal conductivity of the insulation. Using (20) and (22), the thermal resistance between the core and the coolant is obtained as

$$R_{cv(f-w)} = R_{(f-c_p)} + R_{(c_p-w)} \quad (23)$$

In a similar manner, the thermal resistance between the coil and the coolant $R_{cv(c-w)}$ can be also obtained. However, in the heat flow path of the copper losses, there is an additional layer of the insulation material, which is represented as R_{wi} in Fig.7(b).

E. Loading Profile and Energy Yield

The typical wind profile and the power output of a wind turbine over an one year span is shown in Fig. 8. As it is evident from Fig. 8, the power processes by the converter varies in large range and optimizing the inductor for a specific loading condition may result in the suboptimal overall performance. Therefore, instead of optimizing the inductor efficiency at specific loading condition, the energy loss is minimized. In addition to the energy loss minimization, the volume minimization is also considered and multi-objective optimization has been carried out. The energy loss (kWh) per year is calculated using the loading profile and loss modeling and it is used into the optimization algorithm.

F. Optimization Process

The multi-objective optimization has been performed, which minimize a vector of objectives $F(X)$ and returns the optimal parameters values of X.

$$\min F(X) \quad (24)$$

where

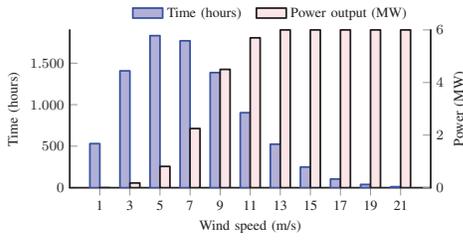$$F(X) = [F_1(X), F_2(X)] \quad (25)$$

Fig. 8. Wind profile and associated output power of a typical 6 MW wind turbine.

TABLE II
VALUES OF L_f AND C_f OF THE LCL FILTER

Parameters	Values
L_f	1200 μH (0.22 pu)
Shunt capacitance $C_f + C_d$	289 μF (0.15 pu)

where $F_1(X)$ returns the energy loss (kWh) and $F_2(X)$ returns the volume of the active parts of the inductor (ltr.). The parameters that are optimized are

$$X = [N \ B_m \ J \ m \ W_c]^T \tag{26}$$

where B_m is the maximum flux density and J is the current density. W_c is the width of the coil (refer Fig. 3(c)). Once the system specifications and the constraints are defined, the optimization has been carried out. As the number of turns N and the number of layers m only take the integer values, mixed-integer optimization problem has been formulated. The steps followed for the optimization process is shown in Fig. 9 and explained briefly hereafter.

1) Step 1: Value of the converter-side inductor L_f: The leakage inductance of the transformer is considered as a part of the grid-side inductor L_g and the use of any additional inductor is avoided. Therefore, the value of the L_g is fixed and the values of the L_f and c_f are obtained while observing the following constraints:

1) $I_h < I_h^*$ where h is the harmonic order ($2 \leq h \leq 180$)
2) Reactive power consumption in shunt branch $\leq 15\%$ of rated power.

The calculated values of the L_f and C_f are listed in Table II.

2) Step 2: Derive dependent design variables: The dependent design variable are derived from the free design variables and the system specifications. The cross-sectional area of the core is obtained as

$$A_c = \frac{L_f I_{max}}{2 N B_m} \tag{27}$$

where I_{max} is the rated current. The dimensions of the core is then obtained as $W_l D_l = A_c/k_s$, where k_s is the stacking factor. For simplicity, $W_l = B_l$ is assumed in this study. The cross-section area of the conductor is obtained as
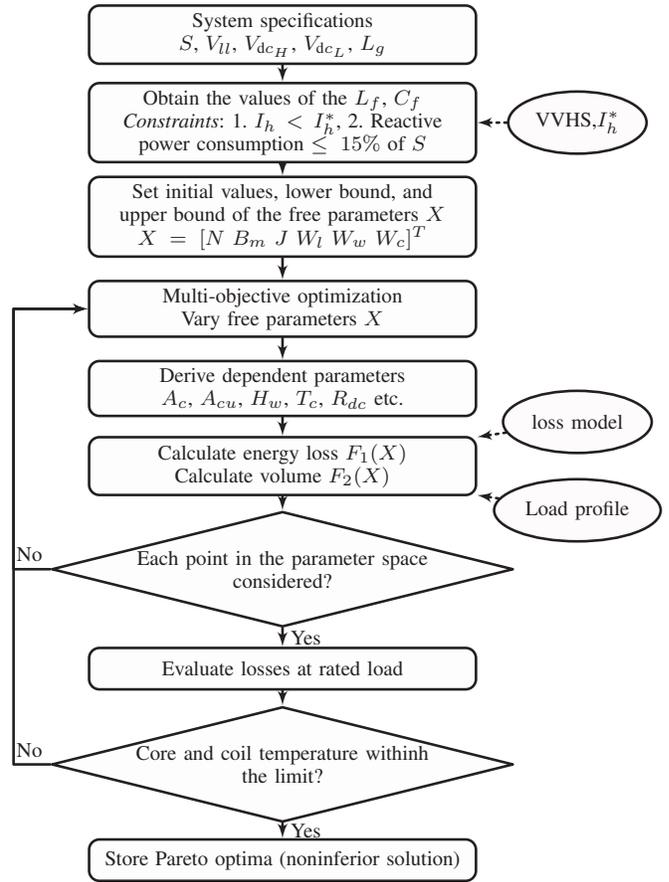
$$A_{cu} = W_c T_c = \frac{I_{max}}{J} \tag{28}$$

Fig. 9. Block diagram, which illustrates the steps of the optimization procedure.

3) Step 3: Objective function evaluation: The objective functions $F_1(x)$ and $F_2(x)$ are evaluated for the given set of parameters and specific mission profile. The core losses and the copper loss for each of the specific loading conditions, shown in Fig. 8, are evaluated. Using this information, the energy loss over one year period is evaluated. Similarly, the volume of both the core and the copper is also calculated.

4) Air gap length: The liquid cooling effectively removes the heat generated due to the copper losses and allows designers to reduce the constant losses (mostly core losses) by increasing the number of turns N. This leads to an improvement in the energy efficiency. However, a larger number of turns also results in larger air gap, which leads to higher fringing flux. The solution is to use several small air gaps, which is achieved by using the discrete core blocks. The length of each of these air gaps and core blocks is limited to 2.5 mm and 30 mm, respectively. If any of these quantities is violated, the solution is discarded.

5) Temperature estimation: The core and the copper losses are evaluated at the rated load conditions and the results are fed to the thermal network shown in Fig. 7(b). By solving the thermal network, temperature of the core (T_{fe}) and the coil (T_{cu}) is obtained. This gives the worst case temperature rise. If
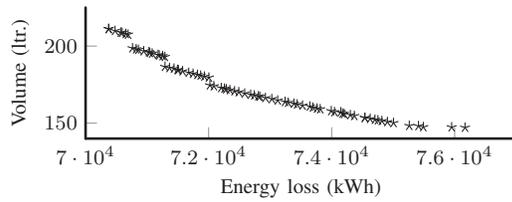
Fig. 10. Calculated volume and energy loss of the integrated inductor for different Pareto optimal solutions.

TABLE III
PARAMETER VALUES OF THE SELECTED DESIGN.

Item	Value	Item	Value	Item	Value
N	25	A_c	30200 mm^2	B_m	1.36 T
W_w	140 mm	J	4.08 A/mm^2	W_c	33 mm
A_{cu}	396 mm^2	H_w	980 mm	k_s	0.92
k_w	0.6	T_c	12 mm	m	2
k_i	0.96	α	1.55	β	1.87

the temperature rise is above the prescribed value, the solution is discarded and the optimization steps are again executed for a new set of free variables.

V. DESIGNED PARAMETERS AND VOLUMETRIC COMPARISON

The energy loss and the volume of the inductor are closely coupled and competes with each other. For example, In a given system, the reduction in the volume often leads to the rise in the losses. As a result, there is no unique solution to the optimization problem. A non-inferior (Pareto optimal) solution is obtained as shown in Fig. 10, where the reduction in the energy loss requires increase in the volume. Out of these several possible design solutions, one that suits the application the most, has been selected. The parameter values of the selected design are given in Table III.

The volume of the inductor is 187.1 ltr. and the energy loss over one year span is 72899 kWh. The coils are designed to carry the rated current (1154 A) and can be wound using copper bars. The major harmonic component in the coil current is at 1.8 kHz and at this frequency, the increase in the ohmic losses in the ac resistance of the coil due to skin effect is insignificant. Therefore, the use of the copper bars for the coils is considered.

The core losses and the copper losses at the full load conditions are 7.09 kW and 9.67 kW, respectively. The coolant flow in each of the duct is taken to be 0.06 l/s and the duct diameter D_d is 0.01 m. The inlet temperature of the coolant is assumed to be 20°C. The core temperature at the rated load is calculated to be 74 °C, whereas the temperature of the coil is found to be 86 °C.

A. Volumetric comparison

The magnetic integration leads to a reduction in the size of the inductor. This has been demonstrated by comparing the volume of the integrated inductor with the volume of the inductors in a separate inductor case. The values of the current
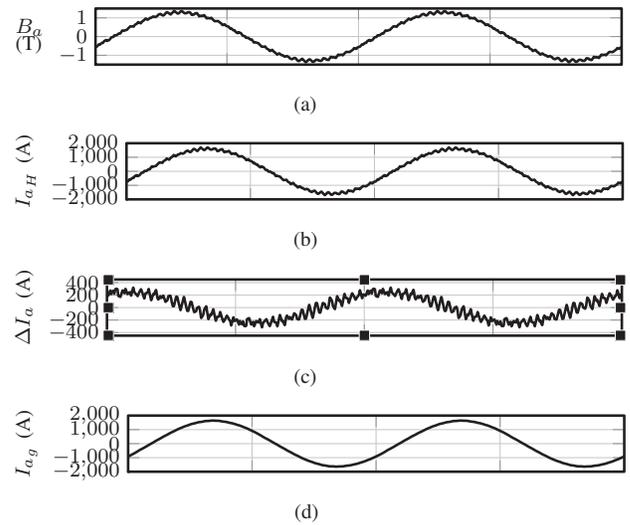

Fig. 11. Simulation results. (a) Flux density waveform in the limb of phase a, (b) Output current of the high-side converter I_h, (c) Current through the shunt branch of the LCL filter, (d) Current through the open-end transformer windings.

Fig. 12. Photo of the implemented inductor.

density of the copper, the maximum flux density in the core and the number of turns N are taken to be the same in both the cases. The volume of the magnetic material of the integrated inductor is calculated to be 132.2 ltr, compared to the 177.3 ltr. for the separate inductors. This demonstrates around 25.4% reduction in the magnetic material, which translates to 314 kg reduction in the weight of the magnetic material (assuming the use of the grain oriented steel).

VI. SIMULATION AND HARDWARE RESULTS

The time domain simulations have been carried out using PLECS. The parameters used in the simulations are specified in Table I. The integrated inductor is modeled using the magnetic toolbox, which uses the permanence model.

The converter is operated at the rated power and the simulated flux density waveform in one of the limb is shown in Fig. 11(a). The output current of the HSC is shown in Fig. 11(b), which has a major harmonic component at 2nd carrier frequency harmonic. The shunt branch of the LCL filter offers low impedance path to the harmonic components, as shown in Fig. 11(c). As a result, the injected grid currents have the desired waveform quality, as shown in Fig. 11(d).

A small scale prototype has been built to verify the effectiveness of the proposed inductor. The specifications of
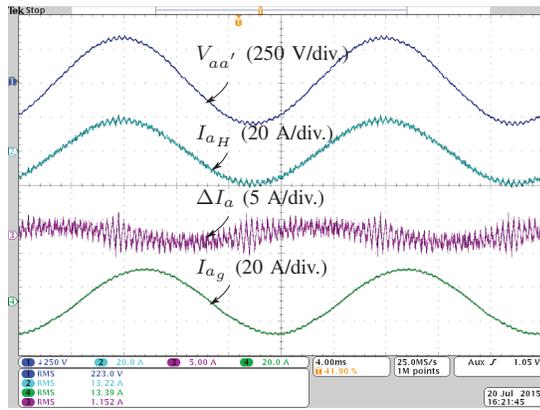
Fig. 13. Experimental results with the system operated at the rated load. Ch1: Voltage across the shunt capacitive branch of phase a of an LCL filter, Ch2: Phase a current of the high side converter, Ch3: Current through the shunt branch of the LCL filter, Ch4: Phase a grid current.
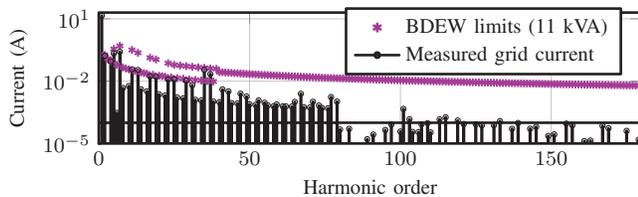

Fig. 14. Harmonic spectra of the measured grid current and associated BDEW harmonic injection limits.

the small scale system is given in Table II. The integrated inductor is realized using the standard laminated steel (0.35 mm) and the coils are wound using the AWG 11. Each coils have 102 turns and the length of the air gap is 2.014 mm. The photo of the inductor prototype is shown in Fig. 12. The converter-side inductance is 9 mH (0.195 pu) and the capacitance of the shunt branch is 24 μF (0.11 pu). The dc-link voltage was derived from the dc power supply and the ac power source from the California Instruments (MX-35) was used to emulate the grid. The converter was operated at the rated load conditions and the experimental results are shown in Fig. 13. The harmonic spectra of the injected current is shown in Fig. 14, where it is evident that the harmonic injection limits are obeyed.

VII. CONCLUSION

An integrated inductor for the the dual-converter fed open-end transformer topology is proposed. The dual-converter system often comprises of two identical VSCs. These two VSCs use two separate converter-side inductors for the LCL filter implementation. For the dual-converter system, the output currents of the given phase of both VSCs are equal. This property of the dual-converter system is exploited to cancel out the flux in one of the yokes of both the inductors through the magnetic integration. Moreover, a multi-objective optimization has been performed to identify best possible solutions which leads to the minimization of the energy loss and minimization

of the volume of the inductor. The size reduction achieved through magnetic integration is demonstrated by comparing the volume of the proposed solution with the separate inductor case. The integrated inductor leads to 25.4% reduction in the volume of the magnetic material. This translates to 314 kg reduction in the weight of the magnetic component for the 6.6 MVA, 3.3 kV WECS system. The performance of the filter has been verified by simulation and experimental studies.

REFERENCES

[1] G. Grandi, C. Rossi, D. Ostojic, and D. Casadei, "A new multilevel conversion structure for grid-connected pv applications," *IEEE Trans. Ind. Electron.*, vol. 56, no. 11, pp. 4416–4426, Nov 2009.

[2] H. Stemmler and P. Guggenbach, "Configurations of high-power voltage source inverter drives," in *Proc. of Fifth European Conference on Power Electronics and Applications*, Sep 1993, pp. 7–14 vol.5.

[3] T. Boller, J. Holtz, and A. Rathore, "Optimal pulsewidth modulation of a dual three-level inverter system operated from a single DC link," *IEEE Trans. Ind. Appl.*, vol. 48, no. 5, pp. 1610–1615, Sept 2012.

[4] N. Bodo, M. Jones, and E. Levi, "A space vector pwm with common-mode voltage elimination for open-end winding five-phase drives with a single DC supply," *IEEE Trans. Ind. Electron.*, vol. 61, no. 5, pp. 2197–2207, May 2014.

[5] M. R. Baiju, K. Mohapatra, R. S. Kanchan, and K. Gopakumar, "A dual two-level inverter scheme with common mode voltage elimination for an induction motor drive," *IEEE Trans. Power Electron.*, vol. 19, no. 3, pp. 794–805, May 2004.

[6] E. Levi, "Multiphase electric machines for variable-speed applications," *IEEE Trans. Ind. Appl.*, vol. 55, no. 5, pp. 1893–1909, May 2008.

[7] F. Blaabjerg, M. Liserre, and K. Ma, "Power electronics converters for wind turbine systems," *IEEE Trans. Ind. Appl.*, vol. 48, no. 2, pp. 708–719, March 2012.

[8] D. G. Holmes and T. A. Lipo, *Pulse Width Modulation for Power Converters: Principles and Practice*. Hoboken, NJ: Wiley-IEEE Press, 2003.

[9] A. Rockhill, M. Liserre, R. Teodorescu, and P. Rodriguez, "Grid-filter design for a multimegawatt medium-voltage voltage-source inverter," *IEEE Trans. Ind. Electron.*, vol. 58, no. 4, pp. 1205–1217, 2011.

[10] "Technical guidline: Generating plants connected to the medium-voltage network." BDEW Bundesverband der Energie- und Wasserwirtschaft e.V., [Online]. Available: http://www.bdew.de, 2008.

[11] G. Gohil, L.Bede, R.Teodorescu, T. Kerekes, and F. Blaabjerg, "Line filter design of parallel interleaved VSCs for high power wind energy conversion system," *IEEE Trans. Power Electron.*, [Online early access], DOI: 10.1109/TPEL.2015.2394460, 2015.

[12] K. Venkatachalam, C. Sullivan, T. Abdallah, and H. Tacca, "Accurate prediction of ferrite core loss with nonsinusoidal waveforms using only steinmetz parameters," in *Computers in Power Electronics, 2002. Proceedings. 2002 IEEE Workshop on*, 2002, pp. 36–41.

[13] J. Li, T. Abdallah, and C. Sullivan, "Improved calculation of core loss with nonsinusoidal waveforms," in *Industry Applications Conference, 2001. Thirty-Sixth IAS Annual Meeting. Conference Record of the 2001 IEEE*, vol. 4, 2001, pp. 2203–2210 vol.4.

[14] A. Hava, R. Kerkman, and T. Lipo, "Simple analytical and graphical methods for carrier-based PWM-vsi drives," *IEEE Trans. Power Electron.*, vol. 14, no. 1, pp. 49–61, Jan 1999.

[15] G. Narayanan and V. T. Ranganathan, "Analytical evaluation of harmonic distortion in PWM AC drives using the notion of stator flux ripple," *IEEE Trans. Power Electron.*, vol. 20, no. 2, pp. 466–474, 2005.

[16] P. Dowell, "Effects of eddy currents in transformer windings," *Proceedings of the Institution of Electrical Engineers,*, vol. 113, no. 8, pp. 1387–1394, August 1966.

[17] W. Hurley, E. Gath, and J. Breslin, "Optimizing the ac resistance of multilayer transformer windings with arbitrary current waveforms," *IEEE Trans. Power Electron.*, vol. 15, no. 2, pp. 369–376, Mar 2000.

[18] G. Gohil, L. Bede, R. Teodorescu, T. Kerekes, and F. Blaabjerg, "An integrated inductor for parallel interleaved three-phase voltage source converters," *IEEE Trans. Power Electron.*, [Online early access], DOI: 10.1109/TPEL.2015.2459134, 2015.

[19] A. V. d. Bossche and V. C. Valchev, *Inductors and Transformers for Power Electronics*. Boca Raton, FL: CRC Press, 2004.